

pubs.acs.org/ac Article

Low-Cost Purpose-Built Ultra-Low-Field NMR Spectrometer

Md Raduanul H. Chowdhury,* Firoz Ahmed, Clementinah Oladun, Isaiah Adelabu, Abubakar Abdurraheem, Shiraz Nantogma, Jonathan R. Birchall, Tobi Abdulbasit Gafar, Yuri A. Chekmenev, Panayiotis Nikolaou, Michael J. Barlow, Boyd M. Goodson, Anton Shcherbakov, and Eduard Y. Chekmenev*



Cite This: https://doi.org/10.1021/acs.analchem.4c03149



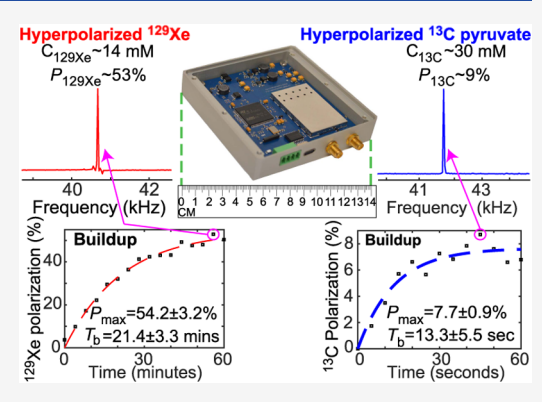
ACCESS

III Metrics & More

Article Recommendations

s Supporting Information

ABSTRACT: Low-field NMR has emerged as a new analytical technique for the investigation of molecular structure and dynamics. Here, we introduce a highly integrated ultralow-frequency NMR spectrometer designed for the purpose of ultralow-field NMR polarimetry of hyperpolarized contrast media. The device measures 10 cm × 10 cm × 2.0 cm and weighs only 370 g. The spectrometer's aluminum enclosure contains all components, including an RF amplifier. The device has four ports for connecting to a high-impedance RF transmit-receive coil, a trigger input, a USB port for connectivity to a PC computer, and an auxiliary RS-485/24VDC port for system integration with other devices. The NMR spectrometer is configured for a pulse-wait-acquire-recover pulse sequence, and key sequence parameters are readily controlled by a graphical user interface (GUI) of a Windows-based PC computer. The GUI also displays the time-domain and Fourier-transformed NMR signal and allows



autosaving of NMR data as a CSV file. Alternatively, the RS485 communication line allows for operating the device with sequence parameter control and data processing directly on the spectrometer board in a fully automated and integrated manner. The NMR spectrometer, equipped with a 250 ksamples/s 17-bit analog-to-digital signal converter, can perform acquisition in the 1–125 kHz frequency range. The utility of the device is demonstrated for NMR polarimetry of hyperpolarized ¹²⁹Xe gas and [1-¹³C]pyruvate contrast media (which was compared to the ¹³C polarimetry using a more established technology of benchtop ¹³C NMR spectroscopy, and yielded similar results), allowing reproducible quantification of polarization values and relaxation dynamics. The cost of the device components is only ~\$200, offering a low-cost integrated NMR spectrometer that can be deployed as a plug-and-play device for a wide range of applications in hyperpolarized contrast media production—and beyond.

■ INTRODUCTION

Low-field (LF) NMR spectroscopy offers an innovative approach for the analysis of molecular structures and reaction dynamics.¹ The distinct advantage of LF NMR lies in its operation at significantly lower frequencies, where digital and analog signal data processing is cheaper and more streamlined.¹ Moreover, low magnetic fields can be readily established by inexpensive small-footprint electromagnets or Halbach array magnets, versus the comparatively large and expensive superconducting magnets usually employed in high-field NMR.²⁻⁴ The field of LF NMR has seen many developments over the years.² Indeed, LF NMR devices have found application in biomedical research,^{5,6} materials science,⁷ environmental studies,⁸ food science,⁹ medical imaging,¹⁰ and many other areas.^{4,11-15}

LF NMR has also been used in NMR hyperpolarization studies. $^{16-22}$ NMR hyperpolarization increases the nuclear spin alignment with the applied magnetic field (termed nuclear spin polarization P) significantly above the thermal equilibrium level. 23,24 Since the detection sensitivity is directly proportional

to the nuclear spin polarization, 25 it follows that the detection sensitivity of LF NMR can be similar or even surpass that of high-field NMR when hyperpolarized contrast media are utilized. 26,27 This feature becomes possible because in HP NMR the nuclear spin polarization is not endowed by the field of the primary magnet (B_0) . 26

There is a wide range of NMR hyperpolarization techniques, including Dynamic Nuclear Polarization (DNP), ^{28–30} Signal Amplification By Reversible Exchange (SABRE) and SABRE in SHield Enables Alignment Transfer to Heteronuclei (SABRE-SHEATH), ^{31–35} Spin Exchange Optical Pumping (SEOP), ^{29,36,37} and ParaHydrogen Induced Polarization (PHIP). ^{38,39} DNP is the most developed and widely used

Received: June 19, 2024
Revised: September 24, 2024
Accepted: September 25, 2024



technique, which utilizes microwave irradiation of free-radical electrons followed by electron spin polarization transfer to target nuclei, e.g. ¹³C.^{28–30} A variant of DNP known as dissolution DNP (d-DNP)³⁰ enhances polarization levels through an additional dissolution process of frozen hyperpolarized contrast agent. In SEOP, the electronic spin angular momentum of an alkali intermediary (e.g., rubidium) is transferred to the target nucleus of a noble gas (typically ¹²⁹Xe, ⁴⁰ which is also employed in this work) via gas-phase collisions, in the presence of circularly polarized laser light.³⁷ In PHIP, the spin angular momentum of parahydrogen (p-H₂) is transferred to an unsaturated substrate via a fast hydrogenation reaction. 38,39 In the SABRE-SHEATH hyperpolarization process (also employed in this work), spin polarization also originates from the p-H₂ molecule. In SABRE-SHEATH a transient polarization transfer catalyst complex is formed between the p-H2-derived hydrides and the catalyst-bound substrate (e.g., [1-13C]pyruvate studied here), resulting in the spontaneous transfer of polarization from the p-H₂-derived hydrides to the target 13 C nuclei. $^{33,41-44}$

The NMR hyperpolarization process is typically performed using a hyperpolarizer device, and *in situ* or *ex situ* NMR polarimetry is utilized to quantify the *P* value and its dynamics, including polarization build-up, decay, and its dependence on specific experimental variables. Moreover, before an HP contrast agent (prepared by any hyperpolarization technique) is administered *in vivo*, NMR polarimetry is greatly desired to confirm the HP agent's potency; i.e., that it has sufficiently high polarization and concentration for the HP scan to be successful with a satisfactory signal-to-noise ratio (SNR). So

A number of ultralow-field (ULF) NMR spectrometer designs have been demonstrated for hyperpolarization detection, and they have their own merits. 3,31-55 However, many spectrometer designs are open-ended for a broad range of applications, whereas purpose-built designs are sometimes desired, e.g., for Nuclear Quadrupolar Resonance (NQR) applications. 12,56 Here, we introduce a miniature (10 cm \times 10 cm \times 2.0 cm), low-cost (\sim \$200 in component cost), ULF (1 to 125 kHz) NMR spectrometer. The capability validation was performed by conducting ULF spectroscopic quantification of produced polarization level, polarization buildup, and relaxation studies of (1) in situ HP ¹²⁹Xe production using SEOP, and (2) ex situ HP [1-13C]pyruvate production using SABRE-SHEATH. We envision that the reported spectrometer can be potentially utilized with other HP techniques⁵⁷ and other ULF applications.¹¹

HP ¹²⁹Xe MRI is a highly sensitive tool for imaging of lung diseases. ^{58–61} The HP ¹²⁹Xe MRI exam has recently received FDA approval for clinical use in lung ventilation imaging in the US. This achievement has further increased the investments from academic and medical institutions, along with ongoing assessments of primary outcome measures to evaluate therapeutic responses. ^{60–62} The HP ¹²⁹Xe gas contrast agent can be produced via batch- or continuous-flow Spin Exchange Optical Pumping (SEOP³⁷) methods. ⁶¹ In this study, we conducted HP ¹²⁹Xe production with a batch-mode hyperpolarizer device. ^{63,64} During the HP ¹²⁹Xe gas production, the *in situ* polarimetry and hyperpolarization dynamics assessment were performed using the Xenon ultimate Spin Exchange (XeUS) ULF NMR spectrometer at a 40.8 kHz resonance frequency.

HP [1-13C]pyruvate has emerged as a next-generation molecular contrast agent, primarily owing to its safety profile

and its central location in metabolic pathways. 65-67 The assessment of pyruvate metabolism has led to remarkable breakthroughs in the identification of cancerous regions within prostate, breast, and brain tissues. 65,66,68 More than 50 clinical trials are underway according to cliniclatrials.gov, employing HP [1-13C]pyruvate as an injectable contrast agent. SABRE-SHEATH hyperpolarization of [1-13C]pyruvate has emerged recently as a new cost-effective (<\$50k)⁶⁹ and ultrafast (1 min) technology⁴³ to produce sufficiently high levels of ¹³C polarization^{70–72} for *in vivo* metabolic imaging.^{73,74} For the present work, HP [1-13C]pyruvate was prepared via SABRE-SHEATH using a benchtop hyperpolarizer operating in microtesla fields.⁶⁹ A 30 mM [1-¹³C]pyruvate sample in methanol was hyperpolarized as described previously, ^{69,70} and the ex situ polarimetry (to measure P_{13C} level, and the dynamics of P_{13C} build-up and decay) was performed using the presented spectrometer, using an electromagnet operating at 3.9 mT, corresponding to 42 kHz ¹³C resonance frequency; the obtained results were compared to those obtained via ex situ 13C polarimetry using a more established technology of benchtop 13C NMR spectrometer operating at 1.4 T, corresponding to 15 MHz ¹³C resonance frequency. ⁴²

■ EXPERIMENTAL SECTION

Design of the ULF NMR Spectrometer. The NMR spectrometer shown in Figure 1a-1d operates from 1 to 125 kHz, and utilizes a pulse-wait-acquire-recover experiment. The spectrometer houses a single receiver channel with a digitally controlled gain of the detected NMR signal. These signal amplifier gain values are +74 dB, + 86 db, and +98 dB. The spectrometer RF input impedance of 1 M Ω , ensuring compatibility with various high-impedance RF coils and experimental setups. The amplified NMR signal is digitized using a 17-bit Analog to Digital Converter (ADC) at 250 kilosamples per second sampling rate. The spectrometer has an internal RF amplifier, capable of delivering up to 160 mW of power in 100 steps (ranging from 1 to 100% settings), and precise control over RF pulse duration (ranging from 1 to 80 half-period pulse durations: for example, at 42 kHz, the pulse length ranges from 11.9 to 952 μ s in increments of 11.9 μ s). The frequency stability of this device is 10 ppm. The spectrometer power is supplied via a USB-C connection of a PC or through an external +24 VDC source. The spectrometer aluminum body measures 10 cm \times 10 cm \times 2.0 cm and weighs 370 g. The overall device schematic is shown in Figure 1e.

The device has two communication options: USB-C and RS-485, which are marked as USB and EXT in Figure 1d. The spectrometer connects to a PC computer via USB-C by using the Windows 10 operating system. An intuitive graphical user interface (GUI, for control of the NMR experiment) and PC-based spectrometer software are developed for Windows 10, Figures 2a,b. Moreover, the USB-C port can be used for device firmware updates using DFU software (Dfuse Demo v3.0.5, STMicroelectronics). The RS-485 communication extends the capabilities to command line operations, enabling further control of the acquisition parameters, aiding in experimental automation integration (to be discussed in future publications).

NMR acquisition parameters can be loaded either through the GUI (via USB-C) or via the command line through RS-485 communication. When operated from a PC and following the application of excitation RF pulse, the raw FID data are recorded by the NMR spectrometer and streamed to the PC,

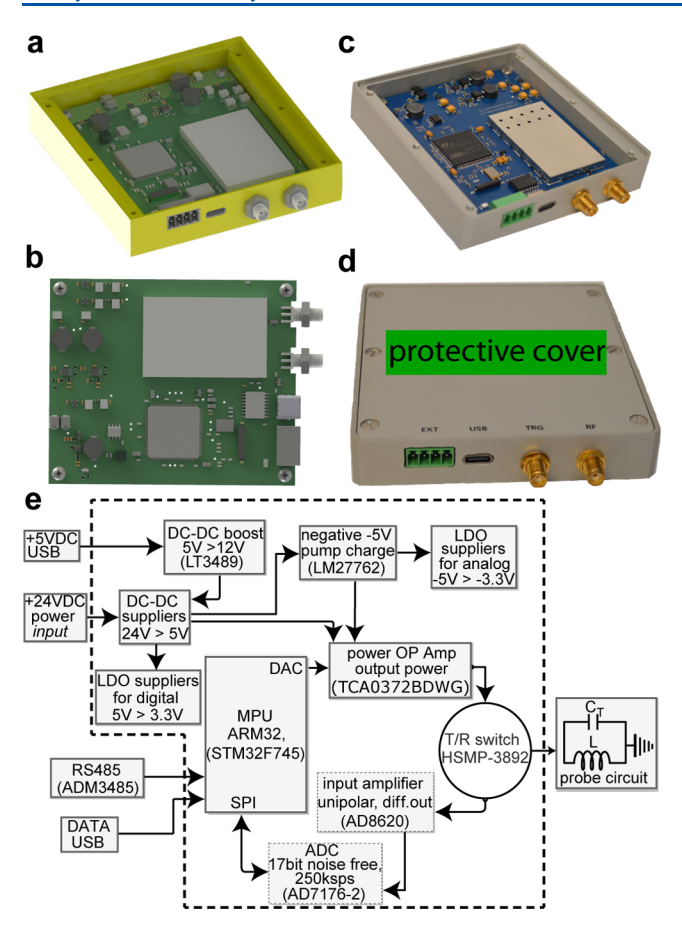


Figure 1. (a) 3D rendering of ULF spectrometer; (b) photograph of the device with the top cover removed; (c) 3D rendering of the printed circuit board (PCB) of the ULF spectrometer (see Figures S2 and S3 for additional close-up views); (d) photograph of the device with the protective cover on (overall dimensions of $10 \text{ cm} \times 10 \text{ cm} \times 2.0 \text{ cm}$); (e) overall block diagram of the ULF spectrometer (see Figure S1 for complete details).

where the custom-made software performs automated data processing to plot the Fourier Transformed (FT) spectrum, identify the highest-intensity data point, integrate the NMR signal, and perform T_2^* analysis. The postprocessing also includes a selection of displayed spectral range for the FT spectrum, line-broadening, and computing full-width-of-halfmaximum (FWHM) of the highest-intensity resonance peak (the detailed discussion of the T_2 * calculations can be found in the section 2.3 of the Supporting Information (SI)). Following the NMR acquisition and data postprocessing, the PC software saves two CSV files containing all the acquisition parameters: one for the time-domain signal and the other one for the FT spectrum. When the spectrometer operates via the RS-485 port, all of the above data processing is performed on the spectrometer directly, and the obtained data can be communicated to other devices via the RS-485 communication protocol. Additional ports, labeled TRG and RF in Figure 1d, are used for NMR pulse-sequence triggering by an external source and to connect the transmit-receive RF coil using SMA connections. The complete schematic of the device, T/R switch arrangement, and PCB layout is shown in Figures S1-\$4 respectively.

The GUI allows for manual control of the following pulse-sequence parameters: number of scans (1-999,999) for signal averaging; transmitter RF pulse frequency (1,000–125,000 Hz

with increment step of 1 Hz); relative RF power (Figure 2d,e); and RF pulse duration. The spectrometer power calibration is performed using an oscilloscope (Figure 2c) by changing the transmitted percent of the power applied during RF pulsing. The details of these calibrations are further discussed in the SI, and also shown in Figure 2c-e. Furthermore, the receiver acquisition time is adjustable from 1 to 131 ms (set values are 1, 2, 4, 8, 16, 33, 66, and 131 ms). The preacquisition delay, recovery time, and spectral region selection range are open for unrestricted input.

Design of ¹²⁹Xe **Polarimetry Studies.** HP ¹²⁹Xe gas was produced by stopped-flow SEOP using a batch-mode generation-2 (GEN-2) clinical-scale ¹²⁹Xe hyperpolarizer device, Figure 2a. ^{47,48,75} Briefly, the device was equipped with a high-power CW pump laser (nominal output \sim 170 W, Bright-Lock Ultra-500, QPC Laser Technologies, Sylmar, CA) equipped with a 2" beam expanding telescope, an \sim 0.5-L SEOP cell (Pyrex cylindrical structure with 2" inner diameter), a high-capacity water chiller (1.4 kW, K-O Concepts DMC-14-G2, Titusville, FL), B_0 electromagnet coil (four-coil Barkerarrangement electromagnet ⁷⁵), power supply for magnet and laser, and an open-source microcontroller (Arduino Mega 2560 rev3, P/N 1050-1018-ND, Digi-key, Thief River Falls, MN). ⁴⁷

A custom-built "butterfly" RF coil was positioned underneath the SEOP cell inside the hyperpolarizer to record the NMR signal from HP 129 Xe in the SEOP cell during the hyperpolarization process, Figure 2b. The RF coil was tuned to 40.8 kHz and connected directly to the spectrometer via SMA cable, Figure 2c and 2d. 47

HP 129Xe gas production was performed at an optimized temperature of 65 °C.47 During this process, a Xe:N2 gas mixture (1:1 mol ratio, 2000 Torr total pressure) was loaded in the SEOP cell. The loaded gas mixture then was irradiated with polarized laser light, and the entire bolus of ¹²⁹Xe gains the HP state over time via a two-step process. Initially, the circularly polarized laser photons were absorbed by Rb metal. Subsequently, the electron spin polarization was transferred to 129Xe noble gas nuclei via gas-phase Rb-Xe atomic collisions. 36,37 In order to sufficiently vaporize the Rb, polarization was performed at a temperature typically ranging from 60 to 80 °C for stopped-flow hyperpolarizer designs.⁶ ¹²⁹Xe polarization increases over time until it reached steady state, where the rates of 129 Xe polarization and T_1 relaxation were in balance. Once the HP state was created, the SEOP cell was cooled to condense the rubidium metal. Following this cell cool-down, NMR spectral data were recorded every 4 min to monitor 129 Xe T_1 relaxation.

Equation 1 was employed to quantitatively convert the recorded signal to $\%P_{\rm Xe}$. Moreover, fitting the polarization buildup data (acquired over the course of 60 min) to a monoexponential model also allowed the measurement of the polarization buildup rate ($\gamma_{\rm SEOP}$). Throughout the NMR data acquisition (both buildup and relaxation), low pulse length (245 $\mu{\rm s}$ (20 half periods) with 66% power setting (63 mW)) was utilized without any substantial HP $^{129}{\rm Xe}$ gas depolarization. 63

Collisions of HP 129 Xe with the inner surfaces of the SEOP cell contributed to the HP gas T_1 depolarization, which was determined largely by paramagnetic centers within the cell walls. The SEOP cell wall was thus protected with a siliconized coating (SurfaSil) to mitigate the effects of these collisions, thereby engendering longer T_1 values and maximizing the

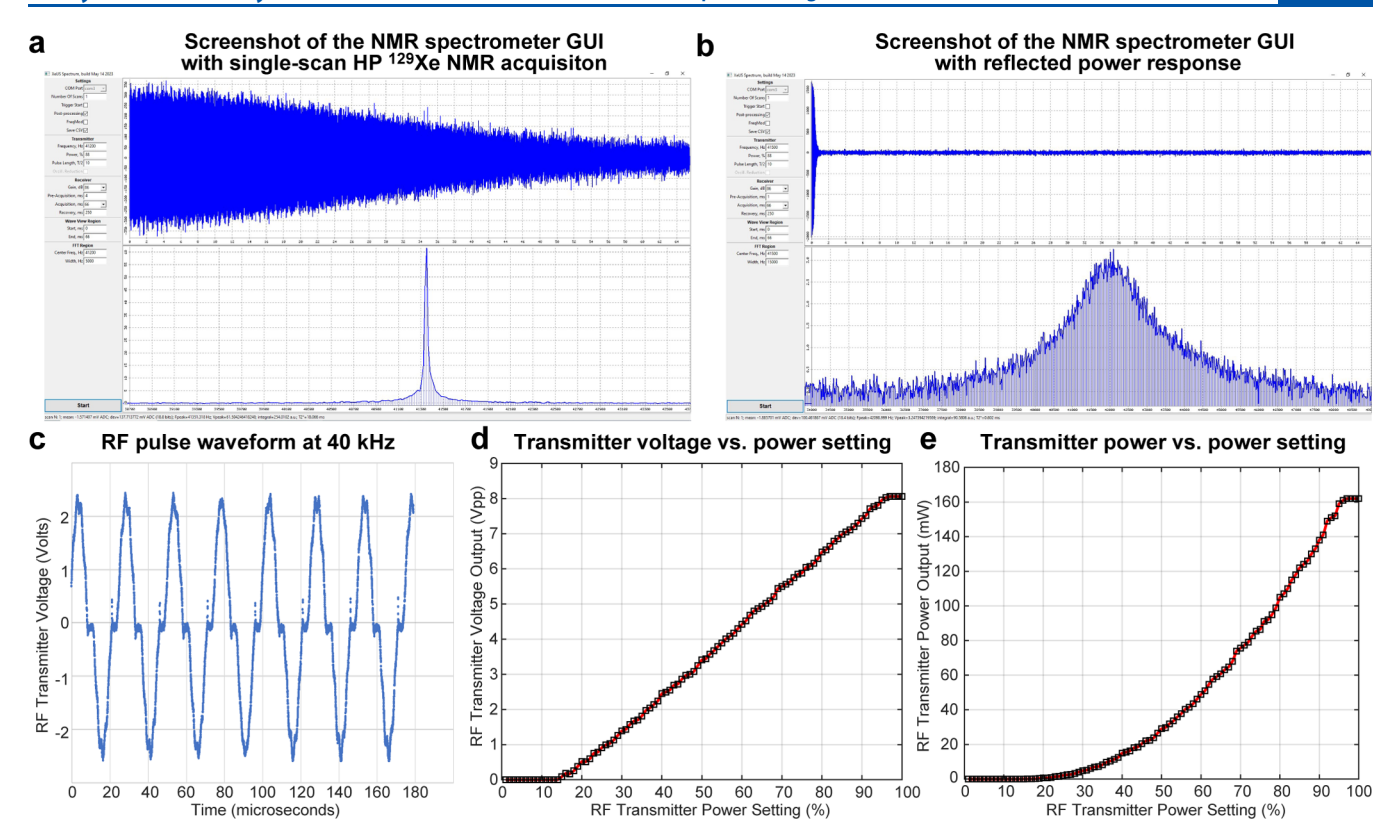


Figure 2. (a) graphical user interface (GUI) of the NMR spectrometer showing an NMR signal acquired during the SEOP of ¹²⁹Xe; (b) corresponding example of acquired reflected power frequency response of the [1-¹³C]pyruvate polarimetry RF coil, operating at 42 kHz. In displays a and b, (left) control menu, (top right) FID, and (bottom right) FT spectrum; (c) RF pulse waveform of the NMR spectrometer transmitter at 40 kHz (recorded using digital oscilloscope); (d) RF transmitter voltage (volts peak-to-peak) as a function of RF pulse transmitter power setting (%); (e) RF transmitter power (milliwatts) as a function of RF pulse transmitter power setting (%).

efficiency of the 129 Xe polarization process. Therefore, the measurement of T_1 relaxation provided information regarding the "health" of the SEOP cell, reflecting the integrity of the surface coating and overall Rb quality. The SEOP cell was replaced once the 129 Xe T_1 value is below 20 min (the condition at which the maximum attainable 6 PXe is substantially decreased), indicating the "end of life cycle" for that SEOP cell

A reference NMR signal obtained from a thermally polarized water sample with an identical geometry allowed the % P_{Xe} value to be calculated using eq 1:

$$P_{Xe} = P_{REF} \left(\frac{C_{REF}}{C_{HP}} \cdot \frac{\gamma_{REF}}{\gamma_{HP}} \cdot \frac{S_{HP}}{S_{REF}} \right) \cdot Corr(T_2^*)$$
(1)

where $P_{\rm REF}$ is the thermal polarization of protons at 40.8 kHz frequency, $C_{\rm REF}$ (110 M) and $C_{\rm HP}$ (14 mM) represented the concentrations of the reference water protons and HP polarized $^{129}{\rm Xe}$ gas, $\gamma_{\rm REF}$ (42.6 \times 10⁶ Hz·T $^{-1}$) and $\gamma_{\rm HP}$ (11.8 \times 10⁶ Hz·T $^{-1}$) were gyromagnetic ratios, and $S_{\rm REF}$ and $S_{\rm HP}$ were peak integral values of signal-reference water protons and HP $^{129}{\rm Xe}$, respectively. The T_2* correction factor ($Corr(T_2*)$) was employed in eq 1 because our measurements employed a significant (usually 4 ms) preacquisition delay and because the T_2* values of the proton reference signal and the HP $^{129}{\rm Xe}$ signal were generally different. 48,49

The reference 1 H signal was obtained from a thermally polarized water sample (doped with 10 mM paramagnetic CuSO₄ to reduce the proton T_1 for more efficient signal averaging) using 190,000 scans (for example, requiring an

"overnight" 16-h-long total scan time; of note the number of averages did not affect P_{Xe} computation as the spectrometer averages the scanned NMR signal). For proton signal acquisition, a 245-µs excitation RF pulse length (i.e., the same pulse duration as the one used for HP ¹²⁹Xe detection) and reduced RF power (35% power setting, corresponding to 8.2 mW) were used, Figure 3e. The reduction of the power level was necessary to match the effective excitation RF B₁ field for both 129Xe and 1H spins by the ratio of the gyromagnetic ratios ($\gamma_{129XE}/\gamma_{1H}$ = 3.6; unfortunately an RF pulse voltage ratio of 2.8X was used in practice accidently (power setting of 66% or 63 mW), which has led to systematic underestimate of ¹²⁹Xe polarization by a factor of 1.1). Note that this water signal was acquired at a lower B_0 magnetic field than HP 129 Xe (but at the same 40.8 kHz resonance frequency) because of the difference in gyromagnetic ratio of ^{1}H and ^{129}Xe ($\gamma_{1H} \approx$

The plot of the % $P_{\rm Xe}$ values versus time (acquired during $^{129}{\rm Xe}$ polarization buildup) exhibited an exponential polarization buildup curve fit, Figure 3g. During HP $^{129}{\rm Xe}$ T_1 relaxation, plotting % $P_{\rm Xe}$ versus time exhibited exponential decay (the T_1 decay experimental time was 60 min), Figure 3h. All the curve fittings were performed using an automated MATLAB code. 76

Design of ¹³**C Polarimetry Studies.** A schematic representation of the HP [1-¹³C]pyruvate SABRE hyperpolarization process is shown in Figure 4a. The SABRE-SHEATH hyperpolarizer setup and the [1-¹³C]pyruvate sample preparation have been described previously, ^{69,71} and

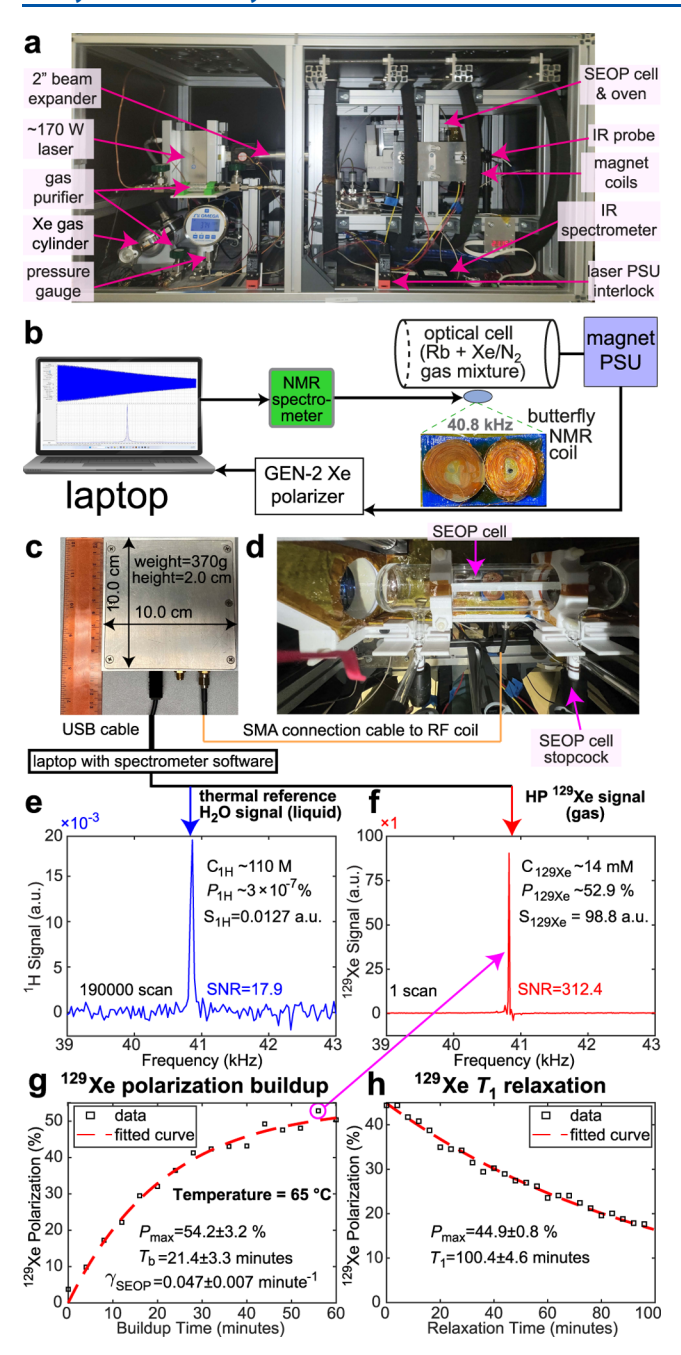


Figure 3. (a) Annotated photographs of second-generation (GEN-2) hyperpolarizer device's open upper chassis with B₀ magnet to show important components required for the SEOP process e.g., SEOP cell, laser (with beam expander), in situ NMR coil, heating jacket, etc. (b) Schematic diagram of the HP ¹²⁹Xe detection process using the XeUS spectrometer. A representative GUI-enabled acquired NMR signal during the in situ NMR polarimetry of HP ¹²⁹Xe using the ULF NMR spectrometer is shown in the laptop window. (c) A photograph of the ULF spectrometer with annotated dimensions and weight. The spectrometer is connected to the RF coil interfacing the SEOP cell jacket via a SMA connection; the spectrometer is also connected to a PC computer via a USB C-type interface that provides power and GUI-enabled features. (d) An annotated photograph of the SEOP cell oven. (e) NMR spectrum of 190,000-scan water ¹H NMR signal detected at 40.8 kHz resonance frequency. (f) Single-shot HP ¹²⁹Xe NMR spectrum detected at 40.8 kHz resonance frequency. (g) ¹²⁹Xe polarization buildup (at 65 °C) and (h) T_1 relaxation at room temperature (25 °C) plotted using NMR acquisition every 4 min.

they are briefly summarized in Figure 4b. This setup allowed bubbling of p-H $_2$ gas through a $[1^{-13}C]$ pyruvate solution (typically methanol-based) in a static (or programmable) submicrotesla magnetic field.

Briefly, the experimental setup of the SABRE-SHEATH process employed a regular 5 mm NMR tube adapted with a 1/4" outer diameter (OD) Teflon tubing jacket, fitted to a push-to-connect wye connector from the hyperpolarizer apparatus. ^{69,77} To initiate the hyperpolarization, 0.6 mL of the [1-¹³C] pyruvate sample (30 mM) with IrIMes catalyst was loaded into the NMR tube and allowed activating for 10 min by bubbling p-H $_2$ through the sample at a flow rate of 130 standard cubic centimeters. A polarization buildup study was performed by bubbling p-H $_2$ through the already-activated sample for different time durations inside the hyperpolarizer magnetic field (optimized to be 0.42 μ T $^{+2}$), until a steady-state 13 C polarization level was reached, Figure 4g and 4i. The total time required for each buildup study (not accounting for sample activation) was approximately 1 h.

First, the detection of the NMR signal from the HP [1-13C]pyruvate sample was performed using a 1.4 T benchtop NMR spectrometer (SpinSolve Carbon, Magritek, Germany) operating at 15 MHz. Next, we employed our ULF polarimetry setup (to be fully described elsewhere in more detail). Briefly, the ULF polarimetry station employed a shielded RF coil operating at 42 kHz frequency. The polarimetry setup featured a B₀ electromagnet coil that generated a homogeneous magnetic field. The coil consisted of four electromagnetic coils (two 199 turns 16.0 cm apart from each other and two 88-turn cols 1.0 cm away from the center coils, using a Barker design arrangement 47,79) where each magnet turn was wound with 18 AWG wire and is positioned between two wooden supports, each measuring 1.0 cm in height (this design is a scaled down version of the previously reported Barker magnet arrangement; 47 specifically, the magnet, diameter, length and wire diameter were scaled down by a factor of 3). The inner diameter of the magnet was 200 mm. The magnet had an inductance of 63.1 mH and a resistance of 9.8 Ω . A 1.86-Amp current was applied to generate an ~4.0 mT field. A small opening at the top-middle section of the coil allowed the NMR tube with the sample to be positioned in the center (most homogeneous part) of the magnet. An RF coil, supported by a 3D-printed support piece, ensured precise positioning of the sample NMR tube for robustness and reproducibility. To detect at 42 kHz frequency using the RF coil (connected to the ULF NMR spectrometer), we used a parallel LC circuit with a resistance of 20 Ω ($X_R = 20 \Omega$), a tuning capacitor of C =33,000 pF with an impedance X_C of ~130 Ω (at 42 kHz), and a multiturn inductor of L = 0.5 mH with an impedance X_L of \sim 130 Ω (at 42 kHz). The RF coil was enclosed with an aluminum cover for shielding. 49,63 A small rectangular opening in the aluminum enclosure allowed one to detect the NMR signal from the sample NMR tube, Figure 4b. The RF coil tuning was performed by adjusting the tuning capacitors of the RF coil circuit and performing spectral analysis of the reflected RF power (by setting the preacquisition time to 1 ms or less), which was too short, allowing detection of the "ringdown" of the RF coil. This reflected power (and the detected NMR signal) was maximal at the RF coil resonance frequency, Figure 4l and Figure 2b.

The acquisition of NMR spectra of HP [1-¹³C]pyruvate employed a single scan, e.g., Figure 4d. Following a given HP sample activation, a corresponding polarization buildup study

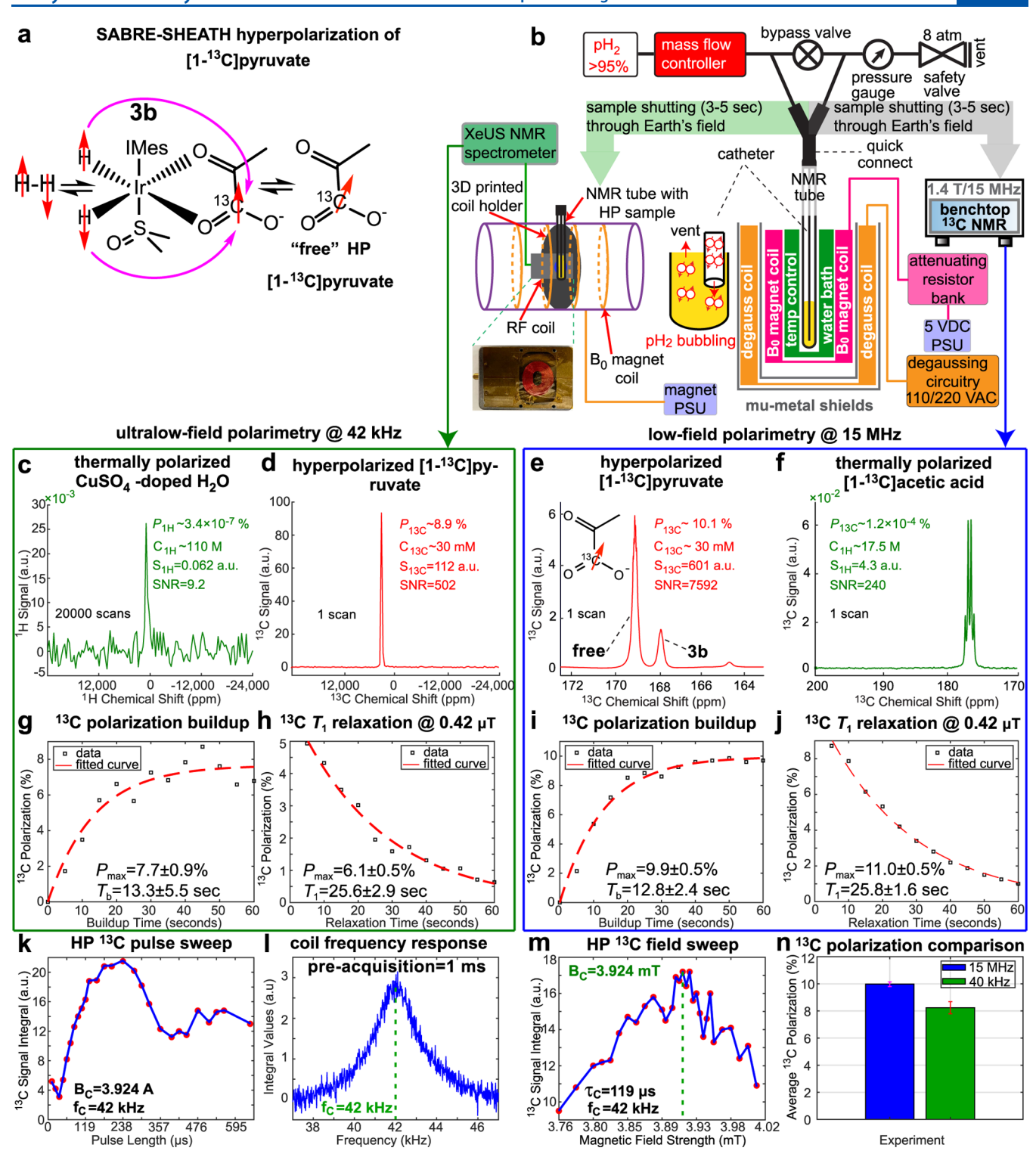


Figure 4. Quantitative ¹³C NMR polarimetry of HP [1-¹³C]pyruvate in CD₃OD using a XeUS spectrometer. (a) Schematic of SABRE-SHEATH hyperpolarization process. (b) Overall schematic of experimental setup of ¹³C hyperpolarization followed by sample transfer to 15 MHz NMR spectrometer or 42-kHz electromagnet-based setups for polarimetry. (c) ¹H NMR of thermally polarized signal-reference water sample (20,000 scans, 110 M) and (d) ¹³C NMR signal of HP [1-¹³C]pyruvate (1 scan, 30 mM) using the ULF spectrometer at 42 kHz (note 12,000 ppm corresponds to approximately 500 Hz). (e) ¹³C NMR signal from HP [1-¹³C]pyruvate (1 scan, 30 mM) and (f) ¹³C NMR signal from signal-reference thermally polarized [1-¹³C]acetic acid (1 scan, 17.5 M) obtained using a 15 MHz benchtop ¹³C NMR SpinSolve NMR spectrometer. (g) ¹³C 13 C 13 C buildup of HP [1-¹³C]pyruvate at 0.42 μ T detected at 42 kHz. (h) ¹³C 13 C 13 C 13 C buildup of HP [1-¹³C]pyruvate at 0.42 μ T detected at 15 MHz. (j) 13 C 13 C acy of HP [1-¹³C]pyruvate at 0.42 μ T detected at 15 MHz. (k) ¹³C RF pulse duration sweep at 42 kHz using the sample of HP [1-¹³C]pyruvate. (l) Frequency response of the RF coil at 42 kHz using preacquisition time of 1 ms, showing the reflected power maximum at a resonance frequency (one scan). (m) ¹³C NMR signal intensity of HP [1-¹³C]pyruvate as a function of B₀ magnetic field current. (n) The comparison between average 9 P_{13C} values obtained from five repeat experiments using 15 MHz (blue: 10.0 ± 0.2%) and 42 kHz (green: 8.4 ± 0.5%) experimental setups, respectively.

was performed, where $\%P_{13\mathrm{C}}$ grew with increasing $p\text{-H}_2$ bubbling time. This exponential increase of $\%P_{13\mathrm{C}}$ was observed until the sample reached steady state polarization. During a given experimental run, the sample was transferred manually from the SABRE-SHEATH hyperpolarizer to either (1) a 15 MHz benchtop setup or (2) a 42 kHz ULF polarimeter setup for NMR detection, Figure 4g and 4i.

Next, a T_1 relaxation study of HP $[1^{-13}C]$ pyruvate was performed by bubbling $p\text{-H}_2$ through the activated sample for 60 s. Following the bubbling, the sample was allowed to depolarize at the 0.42 μ T field for different time durations (each time corresponded to an individual data point) before its immediate transfer to a 15 MHz benchtop NMR spectrometer or 42 kHz ULF polarimeter setup for NMR detection; see Figure 4h and 4j. The total time required for each decay study (not accounting for sample activation) was approximately 1 h.

The polarization quantification of HP [1-13C]pyruvate at 15 MHz was performed by using eq 2. A single scan from a neat thermally polarized [1-13C]acetic acid sample was used as a signal reference, Figure 4f:⁴²

$$P_{13C} = P_{REF} \left(\frac{C_{REF}}{C_{HP}} \cdot \frac{V_{REF}}{V_{HP}} \cdot \frac{S_{HP}}{S_{REF}} \right) \tag{2}$$

where $P_{\rm REF}$ was the thermal polarization of carbon at 15 MHz frequency, $C_{\rm REF}$ (17.5 M) and $C_{\rm HP}$ (30 mM) represented concentrations, $S_{\rm REF}$ and $S_{\rm HP}$ were signal peak integral values, and $V_{\rm REF}$ and $V_{\rm HP}$ were effective solution detection volumes inside the NMR RF coil of the NMR spectrometer (see SI) of signal-reference [1-¹³C]acetic acid and HP [1-¹³C]pyruvate, respectively.

For the ULF setup, eq 3 was used for polarization quantification because the signal from the thermally polarized water protons (doped with $CuSO_4$ to reduce T_1) was utilized in a manner similar to that of HP ¹²⁹Xe studies described above. A 20,000-scan signal-reference spectrum (to boost SNR of thermally polarized protons at 42 kHz) was obtained, Figure 4c.

$$P_{13C} = P_{REF} \left(\frac{C_{REF}}{C_{HP}} \cdot \frac{V_{REF}}{V_{HP}} \cdot \frac{S_{HP}}{S_{REF}} \cdot \frac{\gamma_{REF}}{\gamma_{HP}} \right) \cdot Corr(T_2^*)$$
(3)

where $P_{\rm REF}$ was the thermal polarization of protons at 42 kHz frequency, $C_{\rm REF}$ (110 M) and $C_{\rm HP}$ (30 mM) represented concentrations, $\gamma_{\rm REF}$ (42.6 × 10⁶ Hz·T⁻¹) and $\gamma_{\rm HP}$ (10.7 × 10⁶ Hz·T⁻¹) were gyromagnetic ratios, and $S_{\rm REF}$ and $S_{\rm HP}$ were signal peak integral values of proton signal reference and HP ¹³C scans, respectively. Both proton and ¹³C spectra were recorded at 42 kHz using the same effective RF B_1 value (¹³C power = 88% (130 mW), ¹H power = 35% (8.2 mW); ¹³C/¹H RF pulse voltage ratio = $\gamma_{13\rm C}/\gamma_{1\rm H}$ = 7.2/1.81 = 4.0, Table S4). Moreover, the difference in the rates of transverse signal decay of ¹H and ¹³C was compensated by using a correction factor, $Corr(T_2^*)$ similarly to that in eq 1. Additional details of the calculations for the 42 kHz experiment can be found in section 2.3 of the SI.

■ RESULTS AND DISCUSSION

The NMR spectrometer transmitter RF output exhibits small waveform distortions (Figure 2c), and linear voltage output (from 0 to 8.1 Vpp) in the range of the power settings from 16% to 94%: the corresponding power calibration chart is shown in Figure 3d. Below 16% power setting, the power

transmitted power drops to zero, and there is an amplifier saturation above 94% power setting. Figure 3e shows the corresponding quadratic dependence of the RF output power on the percentage power setting: note the deviation from the expected quadratic relationship below 16% (due to voltage drop) and above 94% (due to saturation).

The performance of the ULF spectrometer was evaluated for NMR polarimetry in two applications: SEOP hyperpolarization of $^{129}\mathrm{Xe}$ gas and SABRE-SHEATH hyperpolarization of $[1^{-13}\mathrm{C}]$ pyruvate. These assessments involved conducting HP NMR signal acquisition for polarization quantification, followed by successive NMR acquisitions during polarization buildup (to measure the $T_{\rm b}$ constant) and relaxation decay (to measure the $T_{\rm 1}$ constant) by using the ULF spectrometer. For the $^{129}\mathrm{Xe}$ SEOP application, these evaluations took place in the 40.8 kHz (3.6 mT) B_0 magnetic field of the GEN-2 hyperpolarizer.

However, for the SABRE-SHEATH experiments, the polarization measurements were performed using two different B_0 magnetic field setups (15 MHz and 42 kHz for 13 C, corresponding to fields of 1.4 T and 3.9 mT, respectively) to enable an additional back-to-back comparison.

In Situ SEOP ¹²⁹Xe Polarimetry Studies. A representative HP ¹²⁹Xe spectrum during polarization buildup is shown in Figure 3f. Comparing the HP spectrum SNR of 312.4 with the signal-averaged reference water scan signal integral (Figure 3e) yields $%P_{Xe} \sim 52.9\%$ according to eq 1.

The HP 129 Xe polarization buildup at the optimized temperature of 65 °C was fit to a monoexponential function, revealing a buildup time constant of $T_b = 21.4 \pm 3.3$ min—corresponding to a buildup rate $\gamma_{\rm SEOP} = 0.047 \pm 0.007$ min $^{-1}$ ($\gamma_{\rm SEOP} = 1/T_b$), Figure 3g. These findings were consistent with previous GEN-2 polarizer studies, which employed a Kea2 NMR spectrometer. The corresponding relaxation dynamics analysis of HP 129 Xe polarization decay shown in Figure 3h yielded the T_1 relaxation time of HP 129 Xe in the SEOP cell of 100.4 ± 4.6 min, affirming the overall "good health" of the SEOP cell.

Based on these findings, it was established that the presented low-cost ULF spectrometer was a viable option for *in situ* polarimetry in ¹²⁹Xe hyperpolarizers. Moreover, the potential integration via the RS-485 command line between the driver and spectrometer can significantly enhance the hyperpolarizer's automation, making it more appealing for clinical research and applications (e.g., ease-of-use without the need for specialist training). Work is in progress in our laboratories toward achieving this goal for next-generation ¹²⁹Xe hyperpolarization instrumentation.

Ex Situ HP [1^{-13} C]Pyruvate Polarimetry Studies. Detection of HP [1^{-13} C]pyruvate NMR signals allowed quantifying the level of 13 C polarization during both polarization buildup and T_1 decay in SABRE-SHEATH studies. Following the hyperpolarization of [1^{-13} C]pyruvate in an optimized submicrotesla field, p-H $_2$ bubbling was stopped and the sample in the NMR tube was transferred to either a low-field (15 MHz) or ULF (42 kHz) setup for further investigation.

Figure 4e and 4f respectively show the acquired NMR signals from single-scan HP [1^{-13} C]pyruvate and thermally polarized [1^{-13} C]acetic acid at 15 MHz using a commercially available benchtop NMR spectrometer, with % P_{13C} = 10.1% for HP [1^{-13} C]pyruvate. For comparison, we conducted the ULF polarimetry at 42 kHz using the presented ULF

spectrometer and using the same sample, p-H2 flow rate, p-H2 bubbling time, and other experimental parameters except that the sample transfer time was ~2 s longer. Figure 4c and 4d respectively show the NMR signals of thermally polarized water (signal reference) and HP [1-13C]pyruvate samples using the ULF spectrometer at 42 kHz, yielding $%P_{13C} = 8.9\%$ for HP [1-13C]pyruvate. This experiment was repeated four more times for each method, yielding an average % P_{13C} of 10.0 \pm 0.2% (with individual values of 10.2%, 10.0%, 10.1%, 9.7%, and 10.0%) for 15 MHz polarimetry and 8.4 \pm 0.5% (with individual values of 8.0%, 8.8%, 8.2%, 8.0%, 8.9%) for 42 kHz polarimetry (Figure 4n). The 15 MHz setup yielded approximately a factor of 1.19 ± 0.06 higher polarization values than the 42 kHz setup, which is likely because the sample transfer from the hyperpolarizer to the 15 MHz detection setup was at least 2 s faster compared to the delivery into the 42 kHz setup; the additional 2-s delay that the sample spent in the Earth's magnetic field $(T_1 \sim 20 \text{ s})$ effectively caused more sample depolarization via T_1 relaxation.

Moreover, the comparison of SNR of the HP $[1^{-13}C]$ -pyruvate spectra showed an SNR of 502 for the ULF setup and 7592 for the 15 MHz setup, demonstrating that the ULF setup was approximately 17 times less sensitive. The key reasons for reduced detection sensitivity were the low sampling rate of 250 kHz in the ULF setup, lower detection frequency and lower field homogeneity (in units of Hz) of the B_0 field in the ULF setup. Potential ways to improve the SNR in these ULF measurements (using this NMR spectrometer) were to increase the resonance frequency of the polarimetry detection and/or increase the reference sample size: Indeed, Figures S16–S17 show the feasibility of detecting the signal from an \sim 50 mL thermally polarized water sample at 90 kHz using only a single scan and an optimized solenoid coil.

Following SABRE-SHEATH polarization of HP [1-13C]pyruvate at 0.42 μ T, we conducted NMR detection in both ultralow-field and low-field to measure both polarization buildup (Figure 4g and 4i) and T_1 relaxation decay (Figure 4h and 4j). The polarization buildup was performed by varying the p-H₂ bubbling time of the sample inside the polarizer. However, for the T_1 measurements, the p- H_2 bubbling was performed for 60 s each time (to establish P_{13} steady state) and then the sample was kept inside the polarizer's magnetic field for different time intervals (e.g., 5 s, 10 s, 15 s, etc.) before sample transfer from 0.42 μT field into a detecting spectrometer for NMR quantification using either the 15 MHz or 42 kHz setup. The polarization buildup T_b for the 15 MHz and 42 kHz measurements was found to be within the margin of error: The $T_{\rm b}$ for the 15 MHz setup was 12.8 \pm 2.4 s (Figure 4i), whereas for the 42 kHz setup it was 13.3 ± 5.5 s (Figure 4g). In terms of the T_1 relaxation values, the results showed 25.8 \pm 1.6 s at 15 MHz and 25.6 \pm 2.9 s at 42 kHz again, well within the margin of experimental error. The T_1 and $T_{\rm b}$ studies demonstrated excellent agreement between the two detection setups, clearly demonstrating the ULF spectrometer's utility for polarization/relaxation dynamics studies.

Outlook. Besides the applications in the area of HP NMR, we envision that the NMR spectrometer maybe potentially utilized for a number of other applications, including teaching the concepts of MR resonance to entry-level students, Nuclear Quadrupolar Resonance (NQR) for the nuclei that resonate within the frequency range of the NMR spectrometer, and low-field relaxometry. The primary limitation of the presented ULF NMR spectrometer is its low upper-frequency cap of 125 kHz,

which reflects compounding limitations of CPU, memory, and ADC. Nevertheless, the design of this purpose-built spectrometer was intended to cater to ultralow-field NMR experiments while also maintaining a low-cost design. Second, the signal detection is limited to 131 ms, corresponding to 8 Hz FWHM spectral resolution, which at 42 kHz corresponds to approximately 190 ppm. Another significant drawback of the spectrometer is the suboptimal SNR, limited by the ADC rate of 250 kHz, as discussed above. As a result of this limitation, signal averaging over a long period of time was necessary on a thermally polarized sample (for example, utilizing 190,000 scans in Figure 4e). Finally, the RF power transmitted output is limited to 0.16 W, which is sufficient for a wide range of ultralow-field NMR applications, but this power cap is likely to become a limiting factor for higher-frequency applications that generally demand substantially more RF excitation power. We anticipate addressing these limitations in a future-generation device that will employ substantially faster CPU, external highpower amplifier, faster and larger capacity RAM and storage components, and faster ADC-indeed, AD9083BBCZ (Analog Devices, 2 Gigasamples/second rate, 16 bit) is readily available (at the cost of \$400), potentially allowing a future design to cover the frequency range of up to 1 GHz, i.e., covering the frequency range of modern high-field MRI scanners and NMR spectrometers. We also envision that such a next-generation low-cost spectrometer may utilize multiple RF transmit and receive channels, gradient channels, external RF amplifier control, RF coil tuning channels, and lower impedance operation, typically preferred for higher-frequency NMR and MRI.

All-in-all, the ULF spectrometer demonstrates robust performance for measurements involving both HP $[1^{-13}C]$ -pyruvate and HP 129 Xe, prepared using SABRE-SHEATH and SEOP hyperpolarization techniques, respectively. This successful demonstration paves the way for using this ULF NMR spectrometer design for experiments with PHIP, d-DNP, and other hyperpolarization techniques.

CONCLUSION

In conclusion, the presented ULF NMR spectrometer has been demonstrated as a versatile, low-cost, and easily accessible instrument tailored for ultralow-field NMR polarimetry applications below 125 kHz. The ultracompact design complemented by its USB-powered plug-and-play convenience and RS-485 integration versality position it as a valuable tool for researchers spanning a wide range of scientific applications in the area of NMR hyperpolarization. The successful utilization of this spectrometer in SEOP hyperpolarization of ¹²⁹Xe gas and SABRE-SHEATH hyperpolarization of [1-¹³C]pyruvate has demonstrated its efficacy in ultralow-field NMR experiments. Specifically, the quantitative assessment of in situ and ex situ polarimetry was demonstrated: the measured $%P_{13C}$ values were additionally quantitatively benchmarked by a secondary NMR detection method: benchtop NMR spectrometer. Based on the outcome of these pilot studies, the spectrometer can be utilized for a rapidly expanding palette of nuclear targets where low-field polarimetry can be particularly valuable, including ¹⁵N, ¹³¹Xe, and many others, which we anticipate in the future. Although certain limitations such as detection range and spectral resolution exist, the prospect of addressing these constraints opens up avenues to expand its applications and democratize access to ultralow-field NMR technology. With ongoing refinements and developments, this

NMR spectrometer design holds the potential to catalyze scientific research and inspire innovation across a multitude of scientific disciplines.

ASSOCIATED CONTENT

Supporting Information

The Supporting Information is available free of charge at https://pubs.acs.org/doi/10.1021/acs.analchem.4c03149.

Additional experimental details, materials and methods including photographs, schematics, figures, tables and additional low-field spectroscopic studies (PDF)

The NMR spectrometer microcontroller firmware and the source code (ZIP)

AUTHOR INFORMATION

Corresponding Authors

Md Raduanul H. Chowdhury — Department of Chemistry, Integrative Biosciences (Ibio), Wayne State University, Karmanos Cancer Institute (KCI), Detroit, Michigan 48202, United States; Email: raduan.acce33.du@gmail.com

Eduard Y. Chekmenev — Department of Chemistry, Integrative Biosciences (Ibio), Wayne State University, Karmanos Cancer Institute (KCI), Detroit, Michigan 48202, United States; orcid.org/0000-0002-8745-8801; Email: chekmenevlab@gmail.com

Authors

Firoz Ahmed – Department of Chemistry, Integrative Biosciences (Ibio), Wayne State University, Karmanos Cancer Institute (KCI), Detroit, Michigan 48202, United States

Clementinah Oladun – Department of Chemistry, Integrative Biosciences (Ibio), Wayne State University, Karmanos Cancer Institute (KCI), Detroit, Michigan 48202, United States

Isaiah Adelabu — Department of Chemistry, Integrative Biosciences (Ibio), Wayne State University, Karmanos Cancer Institute (KCI), Detroit, Michigan 48202, United States; orcid.org/0000-0002-9475-0851

Abubakar Abdurraheem – Department of Chemistry, Integrative Biosciences (Ibio), Wayne State University, Karmanos Cancer Institute (KCI), Detroit, Michigan 48202, United States

Shiraz Nantogma – Department of Chemistry, Integrative Biosciences (Ibio), Wayne State University, Karmanos Cancer Institute (KCI), Detroit, Michigan 48202, United States

Jonathan R. Birchall – Department of Chemistry, Integrative Biosciences (Ibio), Wayne State University, Karmanos Cancer Institute (KCI), Detroit, Michigan 48202, United States

Tobi Abdulbasit Gafar – School of Chemical & Biomolecular Sciences and Materials Technology Center, Southern Illinois University, Carbondale, Illinois 62901, United States

Yuri A. Chekmenev – XeUS Technologies LTD, Nicosia 2312, Cyprus

Panayiotis Nikolaou — XeUS Technologies LTD, Nicosia 2312, Cyprus; ⊚ orcid.org/0000-0002-3802-0803

Michael J. Barlow – Sir Peter Mansfield Imaging Centre, University of Nottingham, Nottingham NG7 2RD, United Kingdom

Boyd M. Goodson — School of Chemical & Biomolecular Sciences and Materials Technology Center, Southern Illinois University, Carbondale, Illinois 62901, United States; orcid.org/0000-0001-6079-5077 Anton Shcherbakov – XeUS Technologies LTD, Nicosia 2312, Cyprus; Custom Medical Systems (CMS) LTD, Nicosia 2312, Cyprus

Complete contact information is available at: https://pubs.acs.org/10.1021/acs.analchem.4c03149

Notes

The authors declare the following competing financial interest(s): P.N., B.M.G., M.J.B., and E.Y.C. declare a stake of ownership in XeUS Technologies, LTD. E.Y.C. serves on the Scientific Advisory Board (SAB) and declares a stake of ownership in Vizma Life Sciences.

ACKNOWLEDGMENTS

This work was supported by DOD CDMRP under W81XWH-15-1-0271, W81XWH-15-1-0272, W81XWH-20-10576, and W81XWH-20-10578, and NSF CHE-1905341, CHE-2404387, CHE-2404388 and CHE-1904780, NIBIB R21 EB033872, and WSU Thomas C. Rumble University Graduate Fellowship (S.N., I.A., A.A., C.O.). B.M.G. acknowledges a Cottrell SEED grant from Research Corporation for Science Advancement. M.J.B. acknowledges financial support from The James Tudor Foundation. We thank Prof. Larry de Graaf and Dr. Wolfgang Kilian for their valuable feedback during the spectrometer development and validation process.

REFERENCES

- (1) Bluemich, B.; Casanova, F.; Appelt, S. Chem. Phys. Lett. 2009, 477 (4-6), 231-240.
- (2) Blümich, B. J. Magn. Reson. 2017, 274, 145-147.
- (3) Michal, C. A. Meas. Sci. Technol. 2010, 21 (10), 105902.
- (4) Michal, C. A. J. Magn. Reson. 2020, 319, 106800.
- (5) Krjukov, E.; Fichele, S.; Wild, J. M.; Paley, M. N. J. Concept Magnetic Res. B 2007, 31B (4), 209-217.
- (6) Coffey, A. M.; Feldman, M. A.; Shchepin, R. V.; Barskiy, D. A.; Truong, M. L.; Pham, W.; Chekmenev, E. Y. J. Magn. Reson. 2017, 281, 246–252.
- (7) Dalitz, F.; Cudaj, M.; Maiwald, M.; Guthausen, G. Prog. Nucl. Magn. Reson. Spectrosc. 2012, 60, 52.
- (8) Downey, K.; Bermel, W.; Soong, R.; Lysak, D. H.; Ronda, K.; Steiner, K.; Costa, P. M.; Wolff, W. W.; Decker, V.; Busse, F.; et al. *Magn. Reson. Chem.* **2024**, *62* (5), 345–360.
- (9) Ezeanaka, M. C.; Nsor-Atindana, J.; Zhang, M. Food Bioproc. Technol. 2019, 12 (9), 1435–1451.
- (10) Prabhat, A. M.; Crawford, A. L.; Mazurek, M. H.; Yuen, M. M.; Chavva, I. R.; Ward, A.; Hofmann, W. V.; Timario, N.; Qualls, S. R.; Helland, J.; et al. Front. Neurol. 2021, 12 (2191), 760321.
- (11) Zalesskiy, S. S.; Danieli, E.; Blümich, B.; Ananikov, V. P. Chem. Rev. 2014, 114 (11), 5641–5694.
- (12) Beguš, S.; Jazbinšek, V.; Pirnat, J.; Trontelj, Z. J. Magn. Reson. **2014**, 247, 22–30.
- (13) Tayler, M. C. D.; Sjolander, T. F.; Pines, A.; Budker, D. J. Magn. Reson. **2016**, 270, 35–39.
- (14) Bouillaud, D.; Drouin, D.; Charrier, B.; Jacquemmoz, C.; Farjon, J.; Giraudeau, P.; Gonçalves, O. *Process Biochemistry* **2020**, 93, 63–68.
- (15) Coffey, A. M.; Shchepin, R. V.; Wilkens, K.; Waddell, K. W.; Chekmenev, E. Y. J. Magn. Reson. 2012, 220, 94–101.
- (16) Coffey, A. M.; Shchepin, R. V.; Feng, B.; Colon, R. D.; Wilkens, K.; Waddell, K. W.; Chekmenev, E. Y. J. Magn. Reson. 2017, 284, 115–124.
- (17) Parnell, S. R.; Woolley, E. B.; Boag, S.; Frost, C. D. Meas. Sci. Technol. 2008, 19, 045601.
- (18) Wong-Foy, A.; Saxena, S.; Moulé, A. J.; Bitter, H.-M. L.; Seeley, J. A.; McDermott, R.; Clarke, J.; Pines, A. J. Magn. Reson. 2002, 157 (2), 235–241.

- (19) Coffey, A. M.; Kovtunov, K. V.; Barskiy, D.; Koptyug, I. V.; Shchepin, R. V.; Waddell, K. W.; He, P.; Groome, K. A.; Best, Q. A.; Shi, F.; et al. *Anal. Chem.* **2014**, *86* (18), 9042–9049.
- (20) Ruset, I. C.; Tsai, L. L.; Mair, R. W.; Patz, S.; Hrovat, M. I.; Rosen, M. S.; Muradian, I.; Ng, J.; Topulos, G. P.; Butler, J. P.; et al. Concept Magnetic Res. B **2006**, 29B (4), 210–221.
- (21) Tsai, L. L.; Mair, R. W.; Rosen, M. S.; Patz, S.; Walsworth, R. L. J. Magn. Reson. 2008, 193 (2), 274–285.
- (22) Zhu, Y.; Chen, C.-H.; Wilson, Z.; Savukov, I.; Hilty, C. J. Magn. Reson. 2016, 270, 71–76.
- (23) Golman, K.; Olsson, L. E.; Axelsson, O.; Mansson, S.; Karlsson, M.; Petersson, J. S. Br. J. Radiol. 2003, 76, S118-S127.
- (24) Nikolaou, P.; Goodson, B. M.; Chekmenev, E. Y. Chem.—Eur. J. 2015, 21 (8), 3156-3166.
- (25) Hoult, D. I.; Richards, R. E. J. Magn. Reson. 1976, 24 (1), 71–85.
- (26) Coffey, A. M.; Truong, M. L.; Chekmenev, E. Y. J. Magn. Reson. **2013**, 237, 169–174.
- (27) Parra-Robles, J.; Cross, A. R.; Santyr, G. E. Med. Phys. 2005, 32 (1), 221–229.
- (28) Becerra, L. R.; Gerfen, G. J.; Temkin, R. J.; Singel, D. J.; Griffin, R. G. Phys. Rev. Lett. 1993, 71 (21), 3561.
- (29) Kovtunov, K. V.; Pokochueva, E. V.; Salnikov, O. G.; Cousin, S. F.; Kurzbach, D.; Vuichoud, B.; Jannin, S.; Chekmenev, E. Y.; Goodson, B. M.; Barskiy, D. A.; Koptyug, I. V.; et al. *Chem.—Asian J.* **2018**, *13* (15), 1857–1871.
- (30) Ardenkjaer-Larsen, J. H.; Fridlund, B.; Gram, A.; Hansson, G.; Hansson, L.; Lerche, M. H.; Servin, R.; Thaning, M.; Golman, K. *Proc. Natl. Acad. Sci. U. S. A.* **2003**, *100* (18), 10158–10163.
- (31) Adams, R. W.; Aguilar, J. A.; Atkinson, K. D.; Cowley, M. J.; Elliott, P. I. P.; Duckett, S. B.; Green, G. G. R.; Khazal, I. G.; Lopez-Serrano, J.; Williamson, D. C. *Science* **2009**, 323 (5922), 1708–1711.
- (32) Salnikov, O. G.; Burueva, D. B.; Skovpin, I. V.; Koptyug, I. V. *Mendeleev Commun.* **2023**, 33 (5), 583–596.
- (33) Iali, W.; Roy, S. S.; Tickner, B. J.; Ahwal, F.; Kennerley, A. J.; Duckett, S. B. *Angew. Chem., Int. Ed.* **2019**, *58* (30), 10271–10275.
- (34) Theis, T.; Truong, M. L.; Coffey, A. M.; Shchepin, R. V.; Waddell, K. W.; Shi, F.; Goodson, B. M.; Warren, W. S.; Chekmenev, E. Y. J. Am. Chem. Soc. 2015, 137 (4), 1404–1407.
- (35) Truong, M. L.; Theis, T.; Coffey, A. M.; Shchepin, R. V.; Waddell, K. W.; Shi, F.; Goodson, B. M.; Warren, W. S.; Chekmenev, E. Y. J. Phys. Chem. C 2015, 119 (16), 8786–8797.
- (36) Walker, T. G.; Happer, W. Rev. Mod. Phys. **1997**, 69 (2), 629–642.
- (37) Walker, T. G. J. Phys. Conf. Ser. 2011, 294, 012001.
- (38) Eisenschmid, T. C.; Kirss, R. U.; Deutsch, P. P.; Hommeltoft, S. I.; Eisenberg, R.; Bargon, J.; Lawler, R. G.; Balch, A. L. *J. Am. Chem. Soc.* 1987, 109 (26), 8089–8091.
- (39) Bowers, C. R.; Weitekamp, D. P. Phys. Rev. Lett. **1986**, 57 (21), 2645–2648.
- (40) Goodson, B. M. J. Magn. Reson. 2002, 155 (2), 157-216.
- (41) Barskiy, D. A.; Shchepin, R. V.; Tanner, C. P. N.; Colell, J. F. P.; Goodson, B. M.; Theis, T.; Warren, W. S.; Chekmenev, E. Y. ChemPhysChem 2017, 18, 1493–1498.
- (42) Adelabu, I.; TomHon, P.; Kabir, M. S. H.; Nantogma, S.; Abdulmojeed, M.; Mandzhieva, I.; Ettedgui, J.; Swenson, R. E.; Krishna, M. C.; Theis, T.; Goodson, B. M.; Chekmenev, E. Y.; et al. *ChemPhysChem* **2022**, 23 (2), 131–136.
- (43) TomHon, P.; Abdulmojeed, M.; Adelabu, I.; Nantogma, S.; Kabir, M. S. H.; Lehmkuhl, S.; Chekmenev, E. Y.; Theis, T. *J. Am. Chem. Soc.* **2022**, *144* (1), 282–287.
- (44) Tickner, B. J.; Semenova, O.; Iali, W.; Rayner, P. J.; Whitwood, A. C.; Duckett, S. B. Catal. Sci. Technol. 2020, 10 (5), 1343–1355.
- (45) Nikolaou, P.; Coffey, A. M.; Walkup, L. L.; Gust, B. M.; Whiting, N. R.; Newton, H.; Muradyan, I.; Dabaghyan, M.; Ranta, K.; Moroz, G.; et al. *Magn. Reson. Imaging* **2014**, 32 (5), 541–550.
- (46) Korchak, S. E.; Kilian, W.; Mitschang, L. Appl. Magn. Reson. **2013**, 44 (1–2), 65–80.

- (47) Birchall, J. R.; Irwin, R. K.; Nikolaou, P.; Coffey, A. M.; Kidd, B. E.; Murphy, M.; Molway, M.; Bales, L. B.; Ranta, K.; Barlow, M. J.; et al. *J. Magn. Reson.* **2020**, *319*, 106813.
- (48) Birchall, J. R.; Irwin, R. K.; Nikolaou, P.; Pokochueva, E. V.; Kovtunov, K. V.; Koptyug, I. V.; Barlow, M. J.; Goodson, B. M.; Chekmenev, E. Y. J. Magn. Reson. 2020, 316, 106755.
- (49) Birchall, J. R.; Nikolaou, P.; Coffey, A. M.; Kidd, B. E.; Irwin, R. K.; Murphy, M.; Molway, M.; Bales, L. B.; Goodson, B. M.; Barlow, M. J.; et al. *Anal. Chem.* **2020**, *92* (6), 4309–4316.
- (50) Saam, B. T.; Conradi, M. S. J. Magn. Reson. 1998, 134, 67-71.
- (51) Kadlecek, S.; Vahdat, V.; Nakayama, T.; Ng, D.; Emami, K.; Rizi, R. NMR Biomed. **2011**, 24 (8), 933–942.
- (52) Ha, D.; Paulsen, J.; Sun, N.; Song, Y.-Q.; Ham, D. Proc. Natl. Acad. Sci. U. S. A. 2014, 111 (33), 11955-11960.
- (53) Krüger, D.; Zhang, A.; Aghelnejad, B.; Hinton, H.; Arnal, V. M.; Song, Y. Q.; Tang, Y.; Lei, K. M.; Anders, J.; Ham, D. *IEEE Journal of Solid-State Circuits* **2023**, 58 (7), 1838–1849.
- (54) Chen, H.-Y.; Kim, Y.; Nath, P.; Hilty, C. J. Magn. Reson. 2015, 255, 100-105.
- (55) Tang, Y.; McCowan, D.; Song, Y.-Q. Sci. Rep. 2019, 9 (1), 11174.
- (56) Hiblot, N.; Cordier, B.; Ferrari, M.; Retournard, A.; Grandclaude, D.; Bedet, J.; Leclerc, S.; Canet, D. C. R. Chimie **2008**, 11 (4), 568-579.
- (57) Eills, J.; Budker, D.; Cavagnero, S.; Chekmenev, E. Y.; Elliott, S. J.; Jannin, S.; Lesage, A.; Matysik, J.; Meersmann, T.; Prisner, T.; et al. *Chem. Rev.* **2023**, *123* (4), 1417–1551.
- (58) Driehuys, B. Acad. Radiol. 2017, 24 (1), 1-3.
- (59) Niedbalski, P. J.; Bier, E. A.; Wang, Z.; Willmering, M. M.; Driehuys, B.; Cleveland, Z. I. *J. Appl. Physiol.* **2020**, *129* (2), 218–229.
- (60) Mugler, J. P.; Altes, T. A. J. Magn. Reson. Imaging 2013, 37 (2), 313-331.
- (61) Khan, A. S.; Harvey, R. L.; Birchall, J. R.; Irwin, R. K.; Nikolaou, P.; Schrank, G.; Emami, K.; Dummer, A.; Barlow, M. J.; Goodson, B. M.; et al. *Angew. Chem., Int. Ed.* **2021**, *60* (41), 22126–22147.
- (62) Walkup, L. L.; Woods, J. C. NMR Biomed. 2014, 27 (12), 1429-1438.
- (63) Birchall, J. R.; Chowdhury, M. R. H.; Nikolaou, P.; Chekmenev, Y. A.; Shcherbakov, A.; Barlow, M. J.; Goodson, B. M.; Chekmenev, E. Y. *Molecules* **2022**, 27 (4), 1327.
- (64) Nikolaou, P.; Coffey, A. M.; Walkup, L. L.; Gust, B. M.; Whiting, N.; Newton, H.; Barcus, S.; Muradyan, I.; Dabaghyan, M.; Moroz, G. D.; et al. *Proc. Natl. Acad. Sci. U. S. A.* **2013**, *110* (35), 14150–14155.
- (65) Qin, H.; Tang, S.; Riselli, A. M.; Bok, R. A.; Delos Santos, R.; van Criekinge, M.; Gordon, J. W.; Aggarwal, R.; Chen, R.; Goddard, G.; et al. *Magn. Reson. Med.* **2022**, 87 (1), 138–149.
- (66) Kurhanewicz, J.; Vigneron, D. B.; Ardenkjaer-Larsen, J. H.; Bankson, J. A.; Brindle, K.; Cunningham, C. H.; Gallagher, F. A.; Keshari, K. R.; Kjaer, A.; Laustsen, C.; et al. *Neoplasia* **2019**, *21* (1), 1–16.
- (67) Goodson, B. M.; Chekmenev, E. Y. Proc. Natl. Acad. Sci. U. S. A. **2024**, 121 (18), No. e2405380121.
- (68) Gallagher, F. A.; Woitek, R.; McLean, M. A.; Gill, A. B.; Manzano Garcia, R.; Provenzano, E.; Riemer, F.; Kaggie, J.; Chhabra, A.; Ursprung, S.; et al. *Proc. Natl. Acad. Sci. U. S. A.* **2020**, *117* (4), 2092–2098.
- (69) Nantogma, S.; Chowdhury, M. R. H.; Kabir, M. S. H.; Adelabu, I.; Joshi, S. M.; Samoilenko, A.; de Maissin, H.; Schmidt, A. B.; Nikolaou, P.; Chekmenev, Y. A.; et al. *Anal. Chem.* **2024**, *96* (10), 4171–4179.
- (70) Schmidt, A. B.; de Maissin, H.; Adelabu, I.; Nantogma, S.; Ettedgui, J.; TomHon, P.; Goodson, B. M.; Theis, T.; Chekmenev, E. Y. ACS Sensors 2022, 7 (11), 3430–3439.
- (71) Nantogma, S.; Eriksson, S. L.; Adelabu, I.; Mandzhieva, I.; Browning, A.; TomHon, P.; Warren, W. S.; Theis, T.; Goodson, B. M.; Chekmenev, E. Y. J. Phys. Chem. A 2022, 126 (48), 9114–9123.

- (72) Ettedgui, J.; Blackman, B.; Raju, N.; Kotler, S. A.; Chekmenev, E. Y.; Goodson, B. M.; Merkle, H.; Woodroofe, C. C.; LeClair, C. A.; Krishna, M. C.; et al. *J. Am. Chem. Soc.* **2024**, *146* (1), 946–953.
- (73) MacCulloch, K.; Browning, A.; Guarin Bedoya, D. O.; McBride, S. J.; Abdulmojeed, M. B.; Dedesma, C.; Goodson, B. M.; Rosen, M. S.; Chekmenev, E. Y.; Yen, Y.-F.; et al. *J. Magn. Reson. Open* **2023**, 16–17, 100129.
- (74) de Maissin, H.; Groß, P. R.; Mohiuddin, O.; Weigt, M.; Nagel, L.; Herzog, M.; Wang, Z.; Willing, R.; Reichardt, W.; Pichotka, M.; et al. Angew. Chem., Int. Ed. 2023, 62 (36), No. e202306654.
- (75) Nikolaou, P.; Coffey, A. M.; Walkup, L. L.; Gust, B.; LaPierre, C.; Koehnemann, E.; Barlow, M. J.; Rosen, M. S.; Goodson, B. M.; Chekmenev, E. Y. J. Am. Chem. Soc. 2014, 136 (4), 1636–1642.
- (76) Birchall, J. R.; Irwin, R. K.; Chowdhury, M. R. H.; Nikolaou, P.; Goodson, B. M.; Barlow, M. J.; Shcherbakov, A.; Chekmenev, E. Y. *Anal. Chem.* **2021**, 93 (8), 3883–3888.
- (77) Joalland, B.; Nantogma, S.; Chowdhury, M. R. H.; Nikolaou, P.; Chekmenev, E. Y. *Magn. Reson. Chem.* **2021**, 59 (12), 1180–1186.
- (78) Cowley, M. J.; Adams, R. W.; Atkinson, K. D.; Cockett, M. C. R.; Duckett, S. B.; Green, G. G. R.; Lohman, J. A. B.; Kerssebaum, R.; Kilgour, D.; Mewis, R. E. *J. Am. Chem. Soc.* **2011**, *133* (16), 6134–6137.
- (79) Barker, J. R. J. Sci. Instrum. 1949, 26 (8), 273-275.